A Novel Fluidized and Induction Heated Microreactor for Catalyst Testing

Mohammad Latifi
Dept. of Chemical and Biochemical Engineering, Faculty of Engineering, Institute for Chemicals and Fuels from Alternative Resources (ICFAR), Western University, London, Ontario, Canada

Dept. of Chemical Engineering, Ecole Polytechnique de Montreal, Montreal, Quebec, Canada

Franco Berruti and Cedric Briens
Dept. of Chemical and Biochemical Engineering, Faculty of Engineering, Institute for Chemicals and Fuels from Alternative Resources (ICFAR), Western University, London, Ontario, Canada

DOI 10.1002/aic.14492

The jiggled bed reactor (JBR) is a state-of-the-art batch fluidized microreactor designed and developed to test catalysts for endothermic reactions. The solid particles in the microreactor are mechanically fluidized by agitating the reactor using a linear pneumatic actuator. An external induction field heats up vertical metal wires installed inside the reactor bed to generate heat rapidly and uniformly within the bed of solid particles, while eliminating hot spots and large temperature gradients. Image and signal processing techniques were utilized to investigate how the fluidization dynamics of the solid particles are affected by the amplitude and frequency of the vibrations, and the size distribution and the mass of the particles. The results show that the microreactor is very flexible: operating conditions can be optimized to successfully fluidize any type of catalyst. Heat-transfer coefficients between heating surfaces and the bed are similar to the coefficients that could be obtained in a well-bubbling fluidized bed. This confirms the excellent quality of the fluidization achieved with the new JBR. © 2014 American Institute of Chemical Engineers *AIChE J*, 60: 3107–3122, 2014
Keywords: endothermic reaction, jiggled bed reactor, fluidization, pneumatic actuator, induction heating

Introduction

Gasification processes are conducted at very high temperatures,[1] where the feedstock is cracked to produce hydrogen and carbon monoxide, which constitute a syngas, the key building block mixture for the production of many valuable chemicals in the petrochemical industry. Steam reforming of natural gas and coal are very common gasification processes. Recent developments of renewable energy resources have opened up new pathways to produce syngas. For example, biomass can be directly converted to syngas. Also, bio-oil, which is the liquid product of biomass pyrolysis, can be gasified to syngas.

Gas–solid fluidized bed reactors offer some advantages, when used for gasification reactions due to higher rates of mass and heat transfer when compared to fixed-bed reactors. Bench scale and pilot plant scale reactors represent appropriate options to investigate the effect of some operating parameters[2] such as temperature, pressure, residence time, steam-to-carbon ratio, and carbon-to-catalyst ratio. However, such reactors are not ideal to test new catalyst formulations for the gasification process as they require relatively large amounts of catalyst. Conversely, suitable microreactors may help reduce the cost of testing various catalyst preparations under ideal conditions.

Currently, available microreactors have some drawbacks. For instance, due to temperature gradients and poor mixing, traditional fixed-bed microreactors may not be able to truly mimic the operating conditions of the industrial reactors. The fluidized bed microreactor technologies available in the market improve mixing. For example, although the SCT-RT is a microreactor which operates batch-wise, it is designed specifically to test catalysts of processes which require a very short residence time like the FCC process.[3] The Berty-style recycle reactors suffer from an axial coke profile due to high recycle rates.[4] The riser simulator[5] overcomes the problem of Berty-style reactors by providing intense gas–solid mixing with an internal impeller above a catalyst basket.

However, a major problem with the current fluidized bed microreactors is the heating method. Gasification processes are endothermic, so enough heat must be supplied to the reactor to sustain the endothermic chemical reactions. In traditional reactors, solids may be conveyed and reheated in a separate vessel, or heat may be transferred from a heat exchanger immersed in the fluidized bed. In contrast, in current test reactors, heat is transferred from the reactor wall to a recirculating gas, with heat-transfer coefficients that are much lower than in a fluidized bed. Therefore, the wall temperature must be maintained significantly higher than the temperature of the catalyst bed, promoting unrealistic

---

Correspondence concerning this article should be addressed to M. Latifi at mohammad.latifi@polymtl.ca.

reactions at the wall. In addition, the volume of the catalyst bed in test reactors such as the riser simulator is much smaller than the total reactor volume. Therefore, for a given residence time, a significant fraction of reactions proceed in the noncatalytic, hot section of the reactor. Moreover, using an impeller operating at high temperature to provide mixing of the solids increases the potential of gas leakage through the mechanical seals and prevents operation at high pressure.

Some heating techniques have been used to attempt to gain information about the temperature profiles inside the test reactors which are similar to those in commercial reactors, such as single pulse shock-tube,[6] light irradiation,[7] and resistive heating.[8] The single pulse shock tube essentially works based on bursting a diaphragm located between high-pressure and low-pressure gas sections. Not only the apparatus should be large but also the shock tube system does not seem to be able to maintain the constant temperature for a long residence time, that is, more than a few milliseconds. Also, the burst diaphragm must be replaced each time with a new one. The light irradiation set up is designed for thermogravimetric studies only in which a concentrated flux of light is beamed to a mass in the focal point of an elliptical mirror. Since each material has different reflective and absorptive properties, these optical parameters must be known to estimate the required flux of the light. Also, since small values of the flux are needed, the short duration of the light pulses must be very well controlled. An alternating current through a wire mesh supplies heat in the resistive heating method and this apparatus is also designed for thermogravimetric studies of pyrolysis. A thermocouple is attached to the wire mesh, but the temperature difference between the wire mesh and the gases in the reactor is not reported.

Induction heating is a heating technique that has been utilized for several applications such as hardening, melting, and welding of conductive materials. The advantage of this heating system is that it is clean, indirect, noncontact, very fast, and precisely controllable.

Induction heating is used to heat up conductive materials with high frequency electrical power, where an AC current passes through a copper coil attached to a power supply.[9,10] Due to the high frequency of the power, the direction of the produced magnetic field around the copper coil alternates very rapidly. The magnetic field induces current on the surface of the conductive material, that is, inside the coil. Varying the direction of the magnetic field also changes the direction of the induced current alternatively, which generates heat. Two types of current can be induced on the surface of the conductive material: the eddy current and hysteresis current. The alternating magnetic field induces eddy currents within the material, whether the material is ferromagnetic or paramagnetic. However, if the conductive material is ferromagnetic and its temperature is below its Curie point, a hysteresis current is also formed: the alternating magnetic field magnetizes and demagnetizes the material crystals, and this rapid switching of magnetic properties causes considerable friction and heating inside the material. The size of the coil and position of the conductive material are important factors to make an effective induction couple to achieve maximum efficiency of the induction heating.[11]

There are very few reports on the application of induction heating to chemical reactors. Rastogi et al. developed a batch microreactor to study the kinetics of propane pyrolysis. To minimize the temperature gradient, ferromagnetic wires with different Curie temperatures were provided inside a magnetic field. These researchers demonstrated that the temperature of the microreactor rapidly reached the Curie point of the corresponding ferromagnetic wire and then remained constant over the period of induction heating.[12] Tsai et al. used induction to heat up a tubular stainless steel reactor in which biomass pyrolysis was taking place. However, they did not report the temperature difference between the reactor wall and its contents.[13]

Initial developments by Rohani et al.[14] indicated that an external induction field can heat up vertical Inconel wires inside a fluidized bed. As a result, the heat is very rapidly generated inside the catalyst bed and efficiently and uniformly distributed throughout the solid particles which are being fluidized, thus, avoiding the creation of hot spots and high-temperature gradients. To prevent shielding of the induction field, the body of reactor cannot be metallic and must be made of ceramic for high-temperature applications.

Effective heat and mass transfer can be achieved by mixing the catalytic bed in a gas fluidized bed reactor; however, such a reactor cannot be used for a batch-wise reactor unless the fluidizing gas is recirculated. Rather than using a fluidizing gas, the catalyst particles can be fluidized mechanically.[15,16] For example, the novel reactor presented in this study uses a linear pneumatic actuator to vertically mix the bed of solids. A major advantage of this method is that it is noninvasive. There are reports of some other applications of mechanical vibration used to enhance the performance of chemical reactors. Klusacek and Schneider[17] achieved a CSTR condition in their reactor with a piston vibrating at 20 Hz with a 3 mm amplitude, which was generated by a commercial loud speaker and an amplifier. Richter et al.[18] used an electromotor attached to a shaft to vibrate their CSTR reactor, but they did not report the frequency and the amplitude of their vibrator. The disadvantage of using an electromotor is that other than being expensive, it is not very flexible, since it is difficult to adjust the frequency and amplitude of the vibrations. Electromagnetic vibrators have also been used for some chemical reactor applications. Squires[19] used an electromagnetic vibrator to investigate axial gas dispersion in laboratory gas–solid reactors. Nelson et al.[20] used an electromagnetic vibrator to fluidize titania-based catalysts for the photo catalytic oxidation of methanol. Although it has been proven that vibrations are an effective technique for fluidization, due to the fact that electromagnetic vibrators operate at very high frequencies of about 20–40 Hz and short amplitudes of 2–4 mm, beds of solid catalyst do not expand entirely inside the reactor. Therefore, secondary reactions would take place in the catalyst-free portion of the reactor. In batch systems, it is desirable to fluidize the catalysts over the entire length of the reactor. It is, therefore, essential to adjust the amplitude and frequency of the vibrations to ensure that the catalyst moves between the two ends of the reactor. In addition, the frequency must be high enough to provide intense mixing of the catalyst with the gas phase and to avoid segregation of particles with different physical characteristics.

The objectives of the work described in this article were the design, construction, operation, and optimization of the fluidization dynamics of a novel, mechanically mixed “jiggled bed” reactor suitable for gasification catalyst testing, and, second, the characterization of the performance of its heating system.

Equipment

The jiggled bed reactor

The objective of the design of the new jiggled bed reactor (JBR) was to provide a well controlled reactor for testing gasification catalysts in a fluidized gas–solid system, where mixing of the catalysts was created by a vibrating motion and the heat required for the endothermic reactions was supplied by induction heating. The JBR includes three sections: the linear pneumatic actuator, the reaction zone, and the induction heating system. The main structure of the JBR is shown in Figure 1.

The gasification reactions take place batch-wise in the JBR. Before injecting the feed, inert gas flushes away any air from the reactor. The feed is then introduced in the reactor through an air lock. At the end of each run, the lower inlet valve and the outlet valve are opened (Valves 1 and 9 in Figure 1), and the reaction products are flushed out by a flow of inert gas into a gas sampling bag.

As induction heating is used to supply the required heat, the reaction chamber is made of a nonconductive material to prevent shielding of the magnetic field. In addition, it is necessary to ensure that it can withstand temperatures as high as 900°C. Moreover, the material must be nonporous and strong enough to sustain the vibrating conditions. Therefore, a nonporous ceramic crucible made of 99.8% alumina is utilized. The crucible has an I.D. of 2.54 cm and a height of 7.3 cm (Figure 2a).

Catalyst particles are fluidized inside the ceramic crucible due to the alternating vertical motion of a linear pneumatic actuator installed below the crucible. This vibrating motion is transferred to the crucible through a scalloped shape stainless steel on top, three stainless steel threaded support rods and a round aluminum seat underneath the crucible, which is mounted directly on the air cylinder of the actuator.

As shown in Figure 2b, the heating element of the JBR is an assembly of eight Inconel wires with a 0.32 cm diameter and a 7.0 cm length, which are attached symmetrically to a round disk made of Inconel. This assembly is inserted from the top, inside the ceramic crucible. When a high frequency current is applied through the copper coil (Item 11 in Figure 1), the associated magnetic field induces a current through the Inconel wires. Due to the high frequency of the magnetic field, the energy of the induced currents is lost rapidly in the form of heat which is transferred from the wires into the bed of catalyst particles.

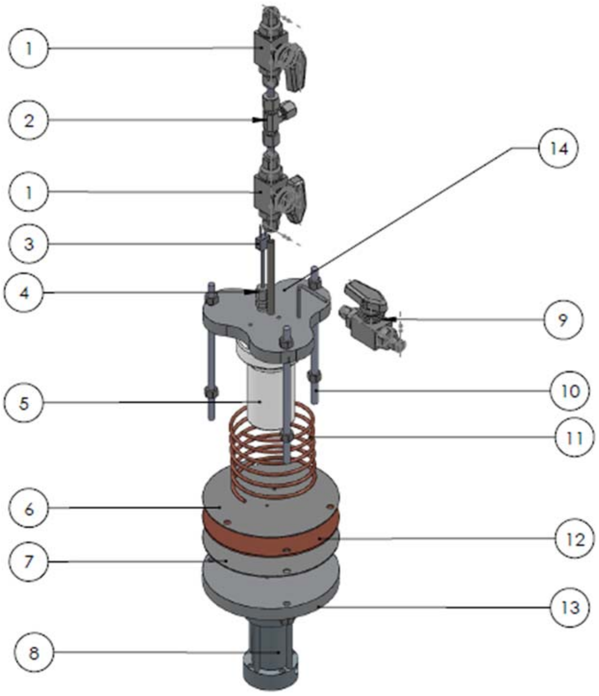

Figure 1. Diagram of the JBR: (1) on/off feed valves; (2) Inlet of carrier gas; (3) Thermocouple; (4) Inlet of feed and carrier gas; (5) Ceramic crucible with insulation; (6) Insulation disk; (7) Insulation disk; (8) Linear pneumatic actuator; (9) Outlet gas valve; (10) Stainless steel support rods; (11) Copper coil; (12) Copper disk; (13) Aluminum disk mounted on the actuator; and (14) Stainless steel scalloped disk.

[Color figure can be viewed in the online issue, which is available at wileyonlinelibrary.com.]

The motion system

To provide good mixing between the solids and gases over the entire length of the ceramic crucible, a linear pneumatic actuator was designed to vibrate the reaction chamber of the JBR with the appropriate frequency and amplitude. This reciprocating motion is transferred to the solid particles inside the ceramic crucible, fluidizing them. The linear pneumatic actuator consists of the following parts (Figure 3):

- Compressed air line.
- A double acting BIMBA FLAT-II air cylinder with dual piston rods and a rod end block to ensure that the rods work in tandem.
- Two BIMBA reed switches (RS) attached on the external surface of the air cylinder to control the motion of the piston.
- A two position, three way solenoid valve to alternate the direction of the compressed air flow between extension and retraction modes.
- Two air flow controllers to adjust the flow rate of the compressed air.
- Tubing between the solenoid valve and the air cylinder.
- A programmed logic controller to start up and shut down the actuator and also to actuate the solenoid valve to alternate the direction of the compressed air flow between extension and retraction modes.

Having dual piston rods in the air cylinder eliminated the need for an external guide to align the movement of the reactor and prevent torsion. A magnet was inserted on the piston so that the RS could sense the position of the piston inside the air cylinder.

To find the optimum size of the air cylinder which could produce vibrations of the desired frequency and amplitude, the effect of mass of the reaction zone of the JBR, distance between the reed switches (RS) and bore size of the air cylinder were investigated (see appendix A). An air cylinder with a 2.7 cm bore size and a 10.16 cm stroke length was, thus, selected as the core of the pneumatic actuator.

The induction heating system

A 9 kW Ameritherm EASY HEAT 7590LI power supply was used to provide high frequency current through the copper coil. The power supply works with a voltage of 187–230

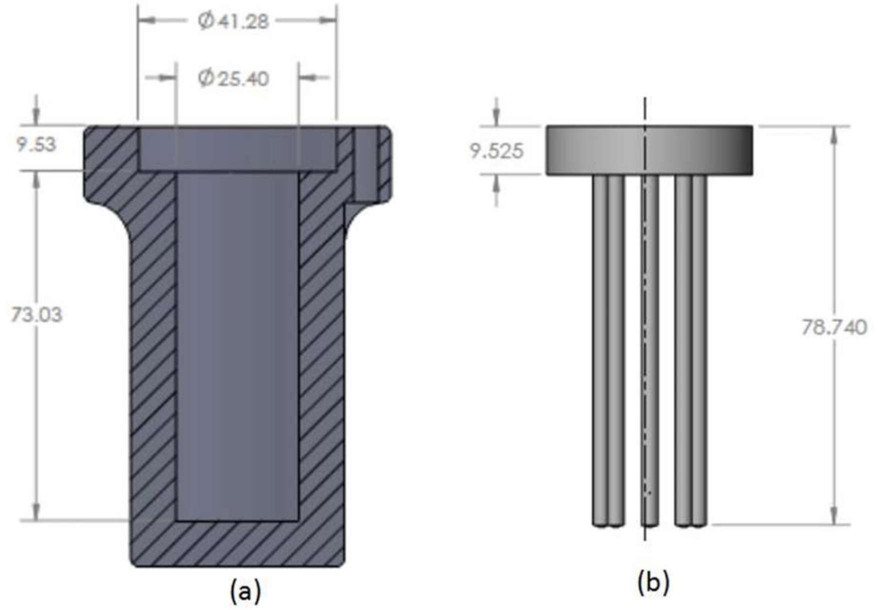

Figure 2. Reaction chamber of the JBR: (a) ceramic crucible and (b) heating element assembly (dimensions are in mm).

[Color figure can be viewed in the online issue, which is available at wileyonlinelibrary.com.]

VAC and its normal achievable frequency is 140–400 kHz, depending on the size of its capacitors as well as the size and design of the induction coil and of the type of conductive metals inside the coil. Cooling water flows through the coil and then discharges from the power supply to prevent the coil from being melted by the high frequency and amperage of the current that flows through it. A UP550 YOKOGAWA controller was used to adjust the induction power to maintain the desired temperature set point within the reactor, which was measured with a type K thermocouple.

The copper coil was made of six turns of a tube with 0.64 cm O.D. Both coil diameter and height were 7.6 cm. An insulation sleeve for electricity was used to cover the external surface of the coil for safety reasons. A high-temperature sleeve was used for the lower turn of the coil where it is in contact with very hot surfaces.

Although the JBR has a fast vibrating motion, the final design implemented included a coil that moved with the ceramic crucible, eliminating any motion between the coil and the internal Inconel wires. This design was selected to avoid any possible variability of the magnetic field which would lead to a nonuniform heating of the internal Inconel wires. Therefore, to deliver the electrical current from the power supply to the vibrating coil, two insulated, conductive flexible tubes with a 91-cm length and a 0.64-cm I.D. connected the coil to the power supply.

Optimization of Fluidization Dynamics—Cold Study

Particle mixing in the JBR

Mixing of the catalyst particles inside the ceramic crucible is induced by the vertical alternating motion of the linear pneumatic actuator. As a result of this motion, the catalyst bed alternately expands and contracts.

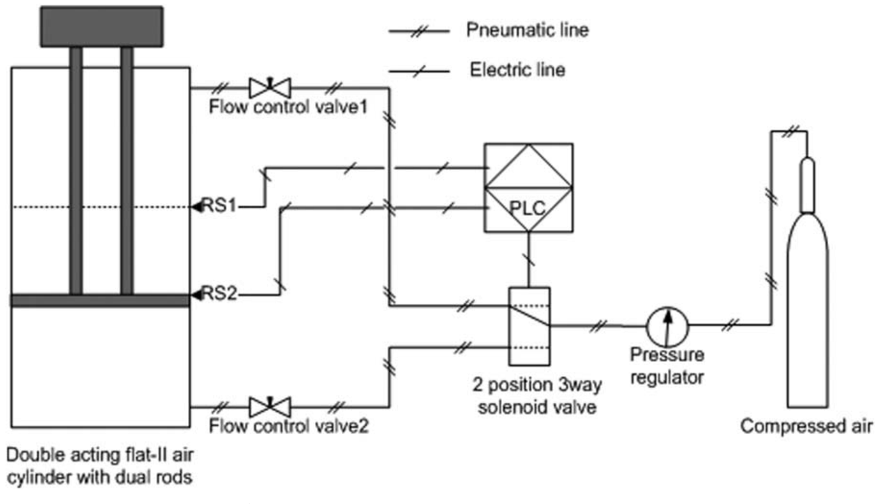

Figure 3. Schematic of the linear pneumatic actuator.

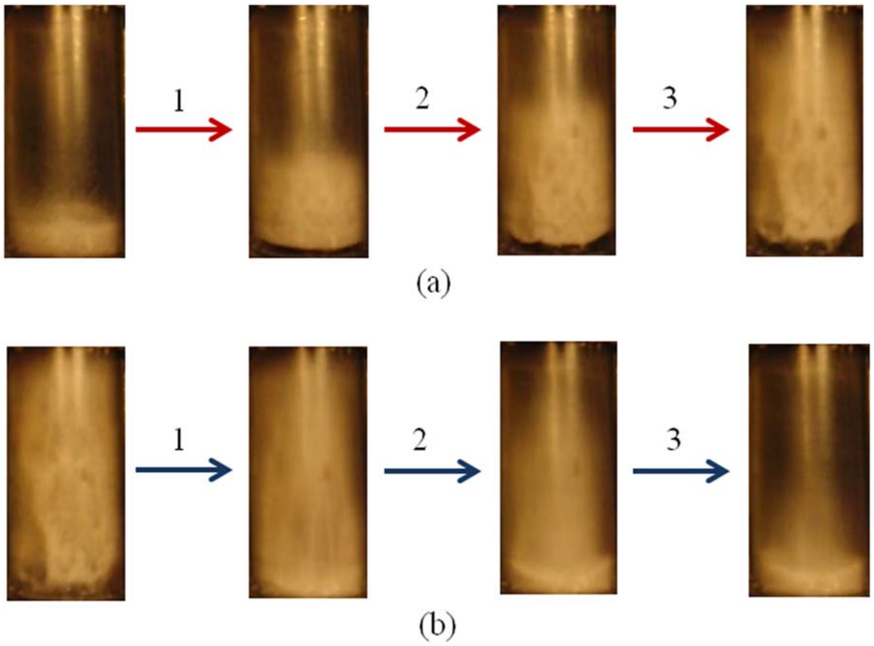

Figure 4. Sequences of mixing of catalyst particles in the JBR: (a) bed expansion during downward actuator retraction and (b) bed contraction during upward actuator extension.

[Color figure can be viewed in the online issue, which is available at wileyonlinelibrary.com.]

When the catalyst bed expands over the entire length of the crucible, the majority of the gas in the upper part of the crucible is displaced downward. When the bed contracts downward, the gas in the lower regions of the crucible is displaced upward. Thus, the alternating expansion/contraction of the catalyst bed induces intense axial and radial mixing of the gas and solid phases. It also promotes heat and mass transfer between the gas and the catalyst particles. Some sequences of the particles mixing are illustrated in Figure 4 when a transparent crucible was used.

To achieve intense mixing, the actuator must be operating with a sufficiently high frequency and amplitude to mix the catalyst particles over the entire length of the ceramic crucible. A systematic study was, therefore, conducted to identify the operating conditions resulting in the catalyst bed expanding over the entire length of the crucible and, overall, in good mixing throughout the microreactor volume.

Experimental set up

A visual set up with a transparent crucible was developed to investigate the uniform distribution of catalyst particles over the entire length of the crucible as a function of the amplitude and frequency of the pneumatic actuator (Figure 5).

Sand particles with a mass of 5, 10, or 20 g, and size distributions of 75–149, 149–212, or 212–355 μm were loaded in a transparent crucible with dimensions similar to those of the ceramic crucible, to form a bed of particles. The pressure of the air driving the actuator was varied between 138 and 690 kPa to adjust the actuator frequency between 3 and 6 Hz. The amplitude of the pneumatic actuator motion was varied between 6.4 and 8.9 cm.

A CASIO EX-FS10 high speed video recording camera, located in front of the transparent crucible (Figure 5) recorded the bed motion. The camera was attached to the crucible frame, so that there was no relative motion between the crucible and the camera. The recording rate of the videos was 210 frames per second. The distance between the camera and the crucible was 13.5 cm. To enhance the contrast of the video recordings, the back of the transparent crucible was wrapped in black tape to provide a dark background contrasting with the light colour of the sand particles. In addition, two 500 W lights illuminated the front of the transparent crucible to improve the video quality.

Viewing the videos in slow motion showed that the catalyst bed reached its minimum height, when the actuator was in its full extension mode. Conversely, the catalyst bed expanded quickly in the crucible when the actuator was in retraction mode. This behavior is caused by the inertia of the catalyst particles, which promotes particles mixing and gas-particles contact.

Image processing methodology

A video to picture conversion software was used to convert the recorded videos, originally in AVI format, to a series of successive pictures, in JPEG format. Pictures showed the catalyst bed every 5 ms.

A MATLAB program was developed to upload the pictures in the RGB (red, green, and blue) color mode and then convert them to gray mode. In gray mode, a single pixel of the picture is described with one gray value between 1 and 256 levels, where 1 corresponds to black and 256 corresponds to white.

For each run, 3000 pictures of a test were uploaded and converted in MATLAB, which correspond to 15 s. To acquire pictures containing the area of the crucible and its content of the sand particles only, a frame around the crucible was cropped from the first picture and then the same area was cropped from other pictures automatically by the program. Since the high speed camera was attached to the

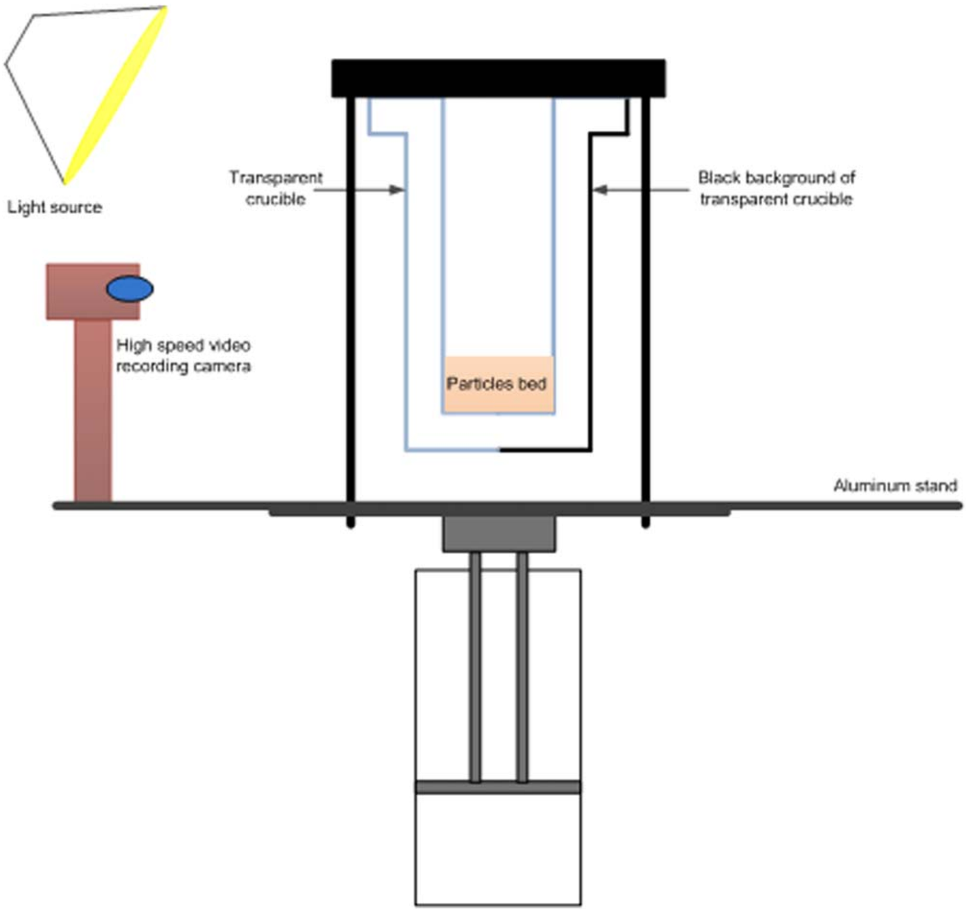

Figure 5. Visual set up to investigate mixing of sand particles in a transparent crucible.

[Color figure can be viewed in the online issue, which is available at wileyonlinelibrary.com.]

crucible stand and did not move relative to the crucible, the coordinates of the area of the cropped frames were the same. The program converted the cropped frame of each picture to a matrix.

To develop a methodology to interpret uniform distribution and fluidization enhancement of the sand particles by image processing, the coefficient of variation of the $y_{i,j}$ pixel gray values was obtained in both space and time coordinates

$$\mathrm{CV}_{\text{space},j} = \left(\frac{\sigma}{\mu}\right)_{\text{space}} = \frac{\sqrt{\frac{1}{N_i}\sum_i\left(y_{i,j}-\frac{\sum_i y_{i,j}}{N_i}\right)^2}}{\frac{\sum_i y_{i,j}}{N_i}} \tag{1}$$

$$\mathrm{CV}_{\text{time},i} = \left(\frac{\sigma}{\mu}\right)_{\text{time}} = \frac{\sqrt{\frac{1}{N_j}\sum_j\left(y_{i,j}-\frac{\sum_j y_{i,j}}{N_j}\right)^2}}{\frac{\sum_j y_{i,j}}{N_j}} \tag{2}$$

where i is the index for space and j is the index for time.

To estimate $\mathrm{CV}_{\text{space}}$ of each cropped frame, the program first calculated $\mathrm{CV}_{\text{space},j}$ for each column of the matrix corresponding to the cropped frame. Then, the average of $\mathrm{CV}_{\text{space}}$ for all the matrix columns was considered as the $\mathrm{CV}_{\text{space}}$ of the related frame.

Preliminary tests showed that $\mathrm{CV}_{\text{time}}$ was a useful indicator of local mixing vs. time on the surface of the catalyst bed, but it did not seem to be related to the fluidization of the solid particles along the length of the crucible. Conversely, $\mathrm{CV}_{\text{space}}$ was a useful indicator to quantify the motion of the catalyst bed along the length of the crucible. As the catalyst bed moved, $\mathrm{CV}_{\text{space}}$ fluctuated and its minimum value, $\mathrm{CV}_{\text{space, min}}$, was found to be corresponded to the maximum bed expansion. Values of $\mathrm{CV}_{\text{space, min}}$ larger than 0.15 were obtained when the catalyst bed did not expand over the entire length of the crucible. Conversely, when the catalyst bed reached the top of the crucible, $\mathrm{CV}_{\text{space, min}}$ became smaller than 0.15.

Figures 6a,b present digitized gray pictures of the sand particles with a mass of 10 g and size distribution of 149–212 μm at two extremes: when the bed is retracted to its minimum height (Figure 6a) and when the bed is expanded over the entire length of the crucible (Figure 6b). Figure 6c presents the corresponding vertical profiles of the horizontal average of pixel gray values. Figure 6c shows the uniform distribution of solids over the crucible length when the bed is fully expanded, while, when the bed is retracted, the sharp drop in pixel gray value from 120 to below 60 corresponds to the volume above the dense bed.

Figure 6c also shows that the pixel gray values are the same at the bottom of the crucible for the retracted bed and over the whole length of the crucible for the expanded bed. This shows that the photographic method, while it could differentiate between various dilute solids concentrations, could not differentiate between high and very high solids concentration. It cannot be used for an accurate measurement of the local solids concentration but is ideal for the analysis of the

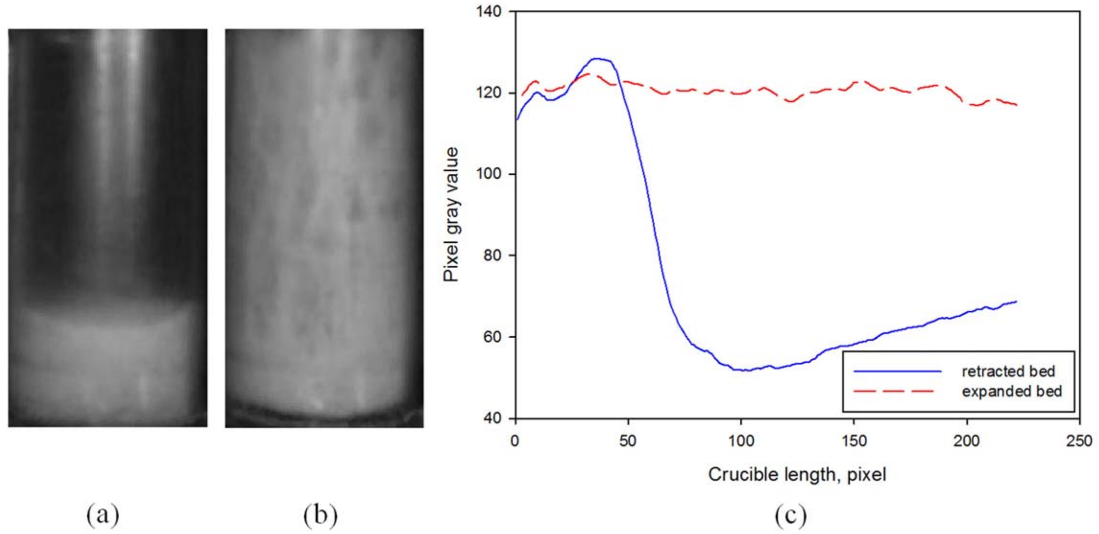

Figure 6. Digitized gray pictures for a bed of the sand particles with 10 g mass and size distribution of 149–212 μm.

Actuator frequency 4 Hz: (a) Retracted bed; (b) Expanded bed; and (c) Variation of the horizontally averaged gray value along the crucible length. [Color figure can be viewed in the online issue, which is available at wileyonlinelibrary.com.]

motion of the surface of the catalyst bed. It also provides information on the mixing of the particles in the denser sections of the bed, by assuming that the particles near the wall are representative of the particles away from the wall, at the same height.

An example of the variation of CV_{space} with time is illustrated in Figure 7 for 10 g of sand particles with size distribution of 149–212 μm and actuator frequency of 4 Hz. Such variation, which was observed in all tested amplitudes and frequencies, is similar to the fluctuations of pressure drop signals from conventional fluidized bed reactors. The variation with time of CV_{space}, therefore, makes it possible to monitor the motion of the catalyst bed.

Therefore, a signal processing program, using the Fourier transform, was used to obtain the power spectrum from the variation with time of CV_{space}, at different amplitudes and frequencies. As an illustrative example, the power spectrum of the bed motion vs. frequency of the bed motion, f_{bed}, which was calculated from the variation with time of CV_{space}, is shown for different pneumatic air pressures with 6.4 cm amplitude in Figure 8 for a 10 g mass of sand particles with a diameter in the range 149–212 μm. For each pressure, there was a clear dominant frequency, $f_{bed,d}$. The dominant frequency provides the frequency of the catalyst bed motion. The power for the dominant frequency, as well, indicates the fluidization intensity. As shown in Figure 8, although the frequency of the bed motion increased following the increase in the actuator air pressure, the maximum power did not follow this trend; in other words, there was an optimum actuator air pressure (representing an actuator frequency) at which the maximum power, and hence the mixing intensity, could be achieved.

Results and discussion

Relation Between the Air Pressure and the Frequency of the Actuator. To estimate frequency of the alternating motion of the pneumatic actuator, the cycles were identified

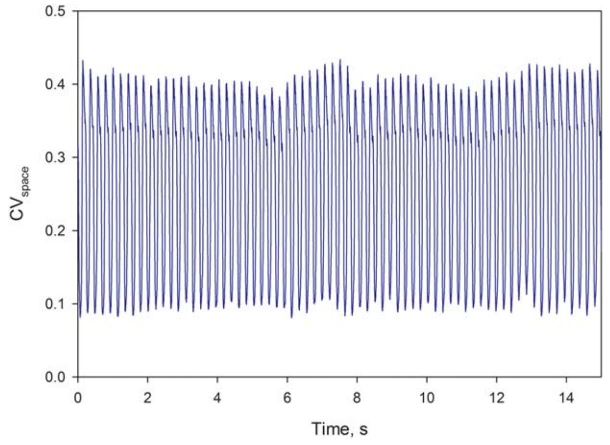

Figure 7. Variation of CV_{space} vs. time; sand particles 10 g, size distribution of 149–212 μm, and air pressure of 345 kPa.

[Color figure can be viewed in the online issue, which is available at wileyonlinelibrary.com.]

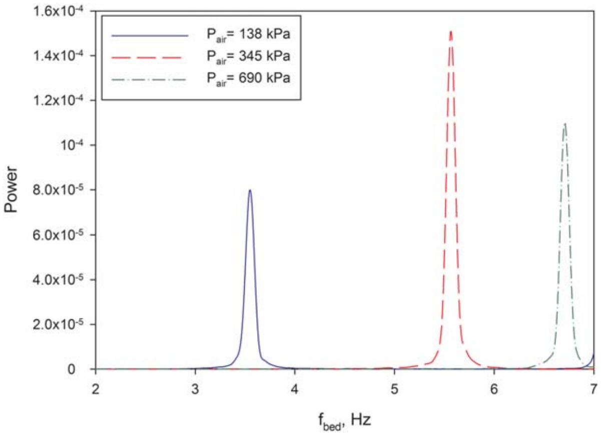

Figure 8. Power spectrum of the bed motion; sand particles 10 g, size distribution of 149–212 μm; and amplitude 6.4 cm.

[Color figure can be viewed in the online issue, which is available at wileyonlinelibrary.com.]

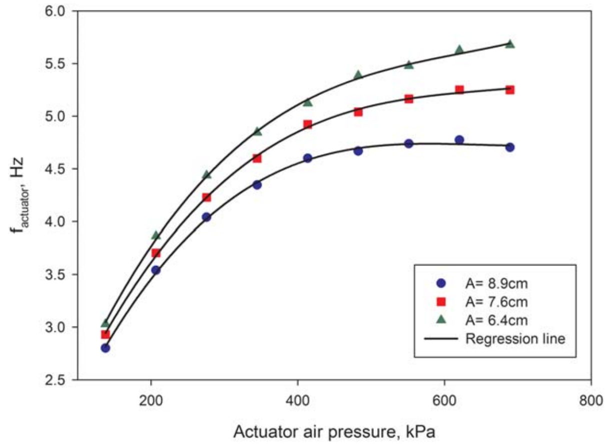

Figure 9. Variation of frequency of the pneumatic actuator vs. air pressure.

[Color figure can be viewed in the online issue, which is available at wileyonlinelibrary.com.]

from the produced frames, and the frequency was estimated using Eq. 3

$$f_{\text{actuator}}\,(\text{Hz}) = \frac{\text{No .of complete cycles}}{\text{No .of frames}} \times \left(\frac{\text{frame}}{\text{second}}\right) \qquad (3)$$

Figure 9 shows variation of the actuator frequency with the air pressure applied to the actuator piston, at amplitudes of 6.4, 7.6, and 8.9 cm. As expected, at a given air pressure, the actuator frequency was lower for a longer amplitude. For given amplitude, the frequency initially increased sharply with increasing air pressure and then plateaued at higher pressures. For the largest amplitude (8.9 cm), the frequency even decreased when the air pressure was increased beyond 600 kPa.

Frequency of the Actuator vs. Frequency of the Bed. It is important to understand whether the catalyst bed fluctuates similar to the frequency of the actuator, slower or faster. This depends on density, size distribution, and mass of the catalyst bed.

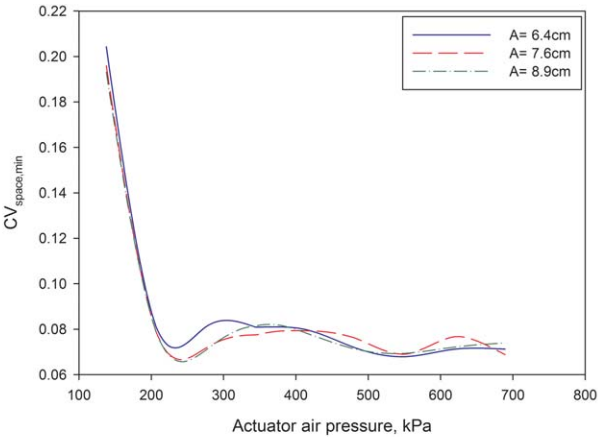

Figure 11. Effect of amplitude on variation of C$V_{\text{space, min}}$ vs. air pressure; sand particles: mass 10 g and size 149–212 μm.

[Color figure can be viewed in the online issue, which is available at wileyonlinelibrary.com.]

Beds of sand particles with 5, 10, and 20 g mass and also with diameters in the ranges 75–149, 149–212, and 212–355 μm, all belonging to Geldart's Group B powders, were tested. The dominant frequency of the bed, which is its significant frequency, is compared with the frequency of the actuator in Figure 10. As shown, the bed vibrated with a higher frequency than the actuator frequency that would be indicating mixing of solid particles not only along the length of crucible but also radially. Results in Figure 10 show that there is a linear relationship between the two frequencies for the bed of sand particles. Furthermore, the relationship between the frequency of the bed and the frequency of the actuator was found independent of the mass and size distribution of the particles inside the reactor according to the results displayed in Figures 10a,b. This observation indicates that displacement of sand particles was quite similar at given actuator frequency regardless of mass and size distribution. On the contrary to displacement of sand particles, as will be presented in Figures 13 and 14, mixing intensity of the bed which is a function of power of the bed frequency was dependent on mass and size distribution.

Effect of the Amplitude of the Pneumatic Actuator Motion on Fluidization. Effect of amplitude of the pneumatic actuator on fluidization dynamics was studied on the bed of sand particles with a mass of 10 g and a diameter ranging from 149 to 212 μm, while the amplitude changed between 6.4, 7.6, and 8.9 cm. These amplitudes were obtained by

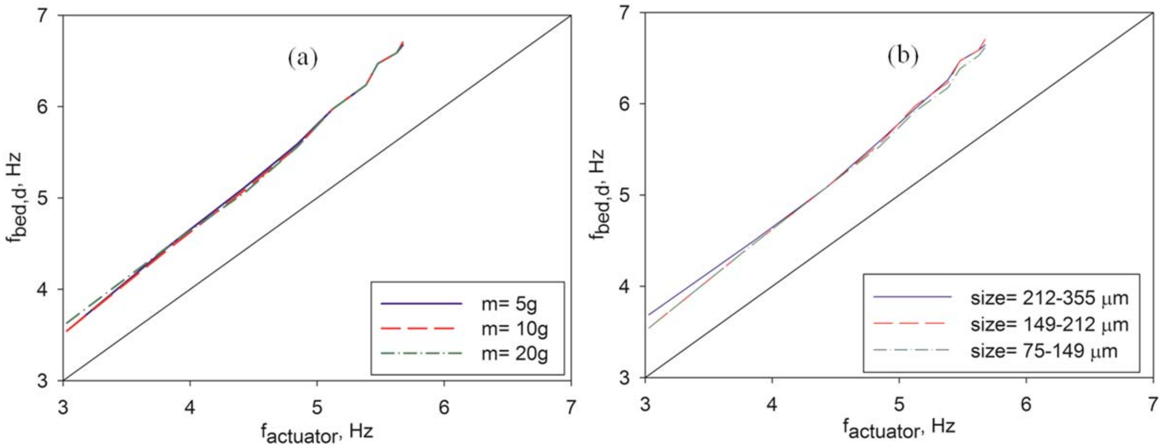

Figure 10. Frequency of bed of the sand particles vs. frequency of the actuator; (a) effect of mass; size 149–212 μm and (b) effect of size distribution; mass 10 g.

[Color figure can be viewed in the online issue, which is available at wileyonlinelibrary.com.]

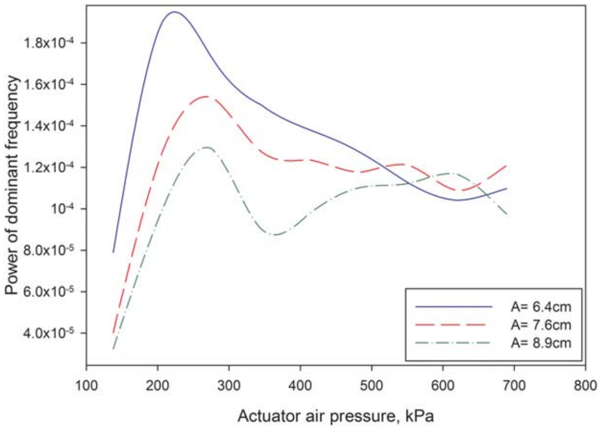

Figure 12. Comparison of power of dominant frequencies vs. air pressure and amplitude; sand particles: mass 10 g and size 149–212 μm.

[Color figure can be viewed in the online issue, which is available at wileyonlinelibrary.com.]

adjusting the distance between the RS on the air cylinder. As explained in Appendix A, the piston inside the air cylinder was travelling a distance longer than the distance between the RS, so it was estimated through the captured high speed videos.

Figure 11 shows that $CV_{space,\ min}$ became less than 0.15, when the air pressure applied to the actuator piston was increased beyond 200 kPa, for all the tested amplitudes and frequencies. This indicates that there was good mixing of the particles as long as the air pressure was above 200 kPa.

However, signals of CV_{space} were further processed to find out the optimum amplitude at which better mixing of solid particles would be provided. Figure 12 compares the variation of the power of the CV_{space} signal with air pressure, for different amplitudes. In general, as the pressure was increased, this power at first increased, peaked and then decreased. Also, as the amplitude was increased, the pressure at which the power peaks increased, while the peak power decreased. The moderate amplitude of 6.4 cm was found to be the optimum amplitude for intense mixing because not only it provided the highest power but also this power was gained at lower actuator frequency.

Effect of Mass and Size Distribution of the Solid Particles on Mixing Intensity. Samples of the sand particles were prepared with size distributions of 75–149, 149–212, or 212–355 μm and were filled in the crucible with masses of 5, 10, or 20 g. The amplitude of the pneumatic actuator was set at 6.4 cm and its frequency was adjusted by varying the air pressure.

In the first step, it was important to figure out whether the bed with different masses would fluctuate over the entire length of the crucible. Results show that except when air pressure was 138 kPa, the $CV_{space,\ min}$ was less than 0.15 and the sand particles were fluidized in the entire length of the crucible when the bed was at maximum expansion of its length. Therefore, there was no significant effect of bed mass of the sand particles on the variation of $CV_{space,\ min}$

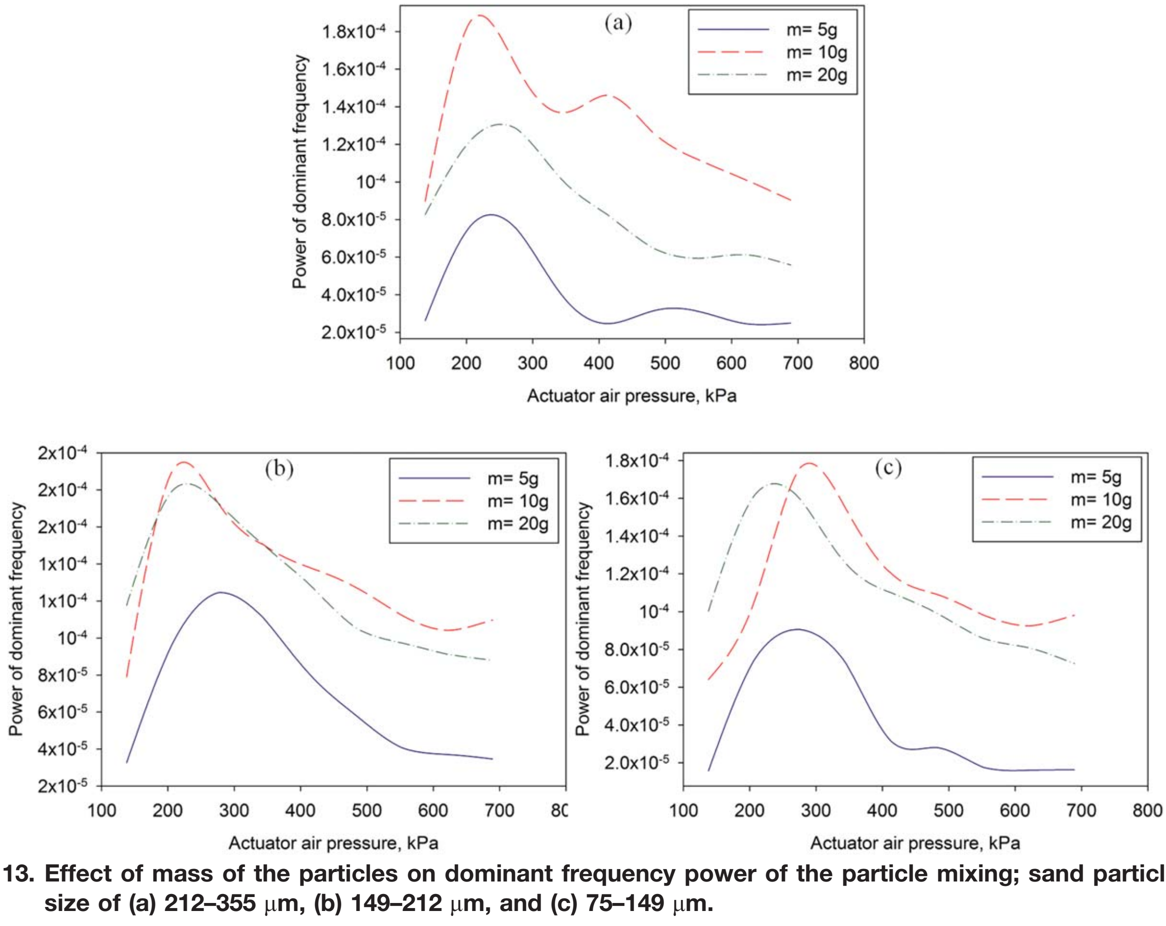

Figure 13. Effect of mass of the particles on dominant frequency power of the particle mixing; sand particles with size of (a) 212–355 μm, (b) 149–212 μm, and (c) 75–149 μm.

[Color figure can be viewed in the online issue, which is available at wileyonlinelibrary.com.]

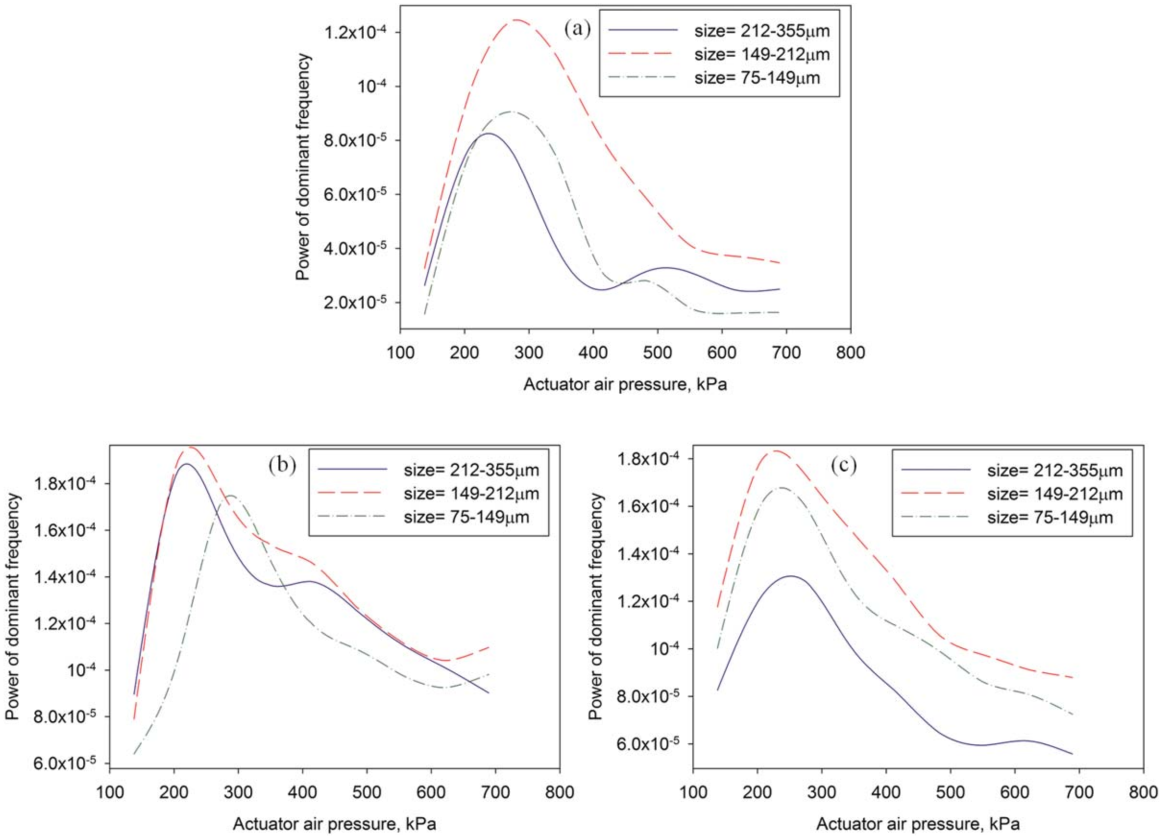

Figure 14. Effect of size distribution of the sand particles on dominant frequency power of the particle mixing; mass of sand particles: (a) 5 g, (b) 10 g, and (c) 20 g.

[Color figure can be viewed in the online issue, which is available at wileyonlinelibrary.com.]

with the air pressure applied to the actuator piston. This means that the results of Figure 11 are valid for all the tested bed masses.

However, analysis of power of dominant frequency revealed that beside effect of the actuator frequency on mixing intensity, the bed mass had a significant impact on the fluidization dynamics. Figure 13 depicts the results for three size distributions. The power of the CV_{space} signal at its dominant frequency changed dramatically with the bed mass. This variation was nonmonotonic, with the highest power being achieved for the intermediate bed mass of 10 g, for all particle-size distributions. With respect to volume of the crucible, 38 cm^3 in our tests, it is, therefore, concluded that there must be an optimum mass of catalyst particles to fill up the volume while achieving maximum mixing intensity.

Therefore, the size distribution of the bed particles also had a significant impact on the fluidization dynamics. Thus, this effect was investigated in more details for masses of 5, 10, and 20 g. Results are shown in Figure 14. The power of the CV_{space} signal at its dominant frequency varied with the size distribution of the bed particles. Interestingly, for all tested bed masses, the highest power was obtained for the intermediate particle size range of 149–212 μm. In general, power of dominant frequencies for the particle size range of

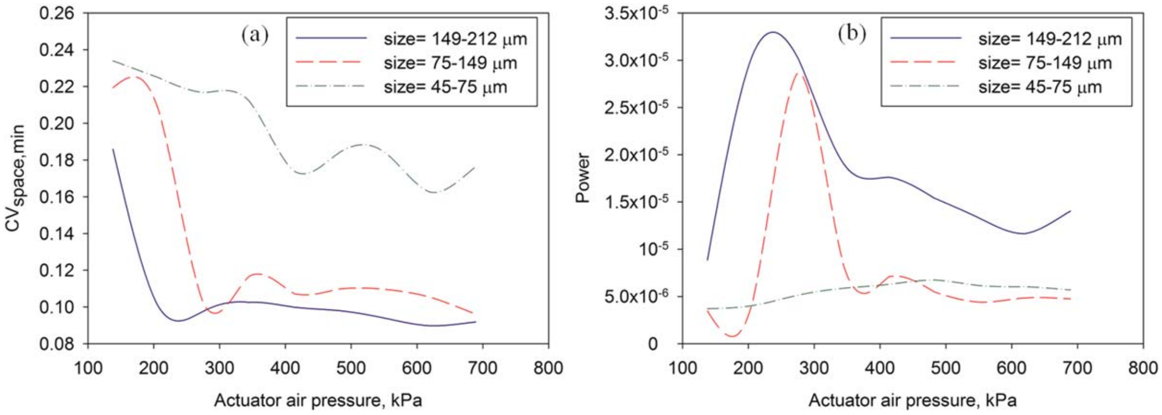

Figure 15. Fluidization of particles of catalyst A representing Geldart's Group A and Group B powders.

[Color figure can be viewed in the online issue, which is available at wileyonlinelibrary.com.]

Table 1. Particle-Size Distribution of Size Cuts of Catalyst A Before Agitation and After Agitation for an Agitation Time of 30 min

$d_{p,BAG} = 742(\mu m)\, d_{p,AAG} = 714(\mu m)$			$d_{p,BAG} = 335(\mu m)\, d_{p,AAG} = 347(\mu m)$			$d_{p,BAG} = 335(\mu m)\, d_{p,AAG} = 347(\mu m)$		
Size (μm)	Wt % BAG	Wt % AAG	Size (μm)	Wt % BAG	Wt % AAG	Size (μm)	Wt % BAG	Wt % AAG
2.6	0.000	0.053	51.5	0.000	0.034	59.0	0.000	0.035
3.0	0.000	0.057	59.0	0.000	0.039	67.5	0.000	0.037
3.4	0.000	0.061	67.5	0.000	0.043	77.3	0.000	0.038
3.9	0.000	0.063	77.3	0.000	0.046	88.6	0.000	0.041
4.5	0.000	0.062	88.6	0.000	0.048	101.5	0.043	0.048
5.1	0.000	0.057	101.5	0.000	0.049	116.2	0.065	0.156
394.2	0.157	0.181	116.2	0.000	0.051	133.1	0.195	0.247
451.6	1.057	1.003	133.1	0.000	0.096	152.5	0.388	0.456
517.2	3.235	3.912	152.5	0.000	0.126	174.6	0.832	0.946
592.4	9.367	11.586	174.6	0.043	0.214	200.0	1.882	2.137
678.5	21.306	24.505	200.0	0.192	0.350	229.1	4.259	4.944
777.1	29.939	29.537	229.1	0.387	0.628	262.4	9.081	10.345
890.1	21.602	18.669	262.4	0.830	1.225	300.5	15.995	16.937
1019.5	8.816	7.312	300.5	1.841	2.558	344.2	20.581	20.118
1167.7	2.901	2.129	344.2	4.127	5.387	394.2	18.577	17.597
1337.5	1.033	0.658	394.2	8.751	10.486	451.6	12.848	12.013
1531.9	0.467	0.159	451.6	15.494	16.784	517.2	7.595	6.959
1754.6	0.119	0.000	517.2	20.198	19.711	592.4	4.059	3.700
			592.4	18.703	16.985	678.5	2.024	1.855
			678.5	13.182	11.436	777.1	0.963	0.895
			777.1	7.790	6.590	890.1	0.507	0.497
			890.1	4.247	3.545	1019.5	0.109	0.000
			1019.5	2.211	1.839			
			1167.7	1.132	0.974			
			1337.5	0.620	0.541			
			1531.9	0.253	0.214			

212–355 μm was the lowest among all tested particle sizes. Similarly, the lower power of dominant frequency for the size range of 75–149 μm than for the size range of 149–212 μm could be attributed to lighter weight of finer particles that effects their motion during the bed contraction.

The conclusion that can be drawn from the results illustrated in Figures 13 and 14 is that it is always possible to find optimum bed mass, particle-size distribution, and actuator frequency at which maximum mixing intensity is achievable. Regarding sand particles, it is best to use a bed of 10 g with a 149–212 μm particle-size distribution. It is also preferable to operate the actuator piston with an air pressure slightly above 200 kPa.

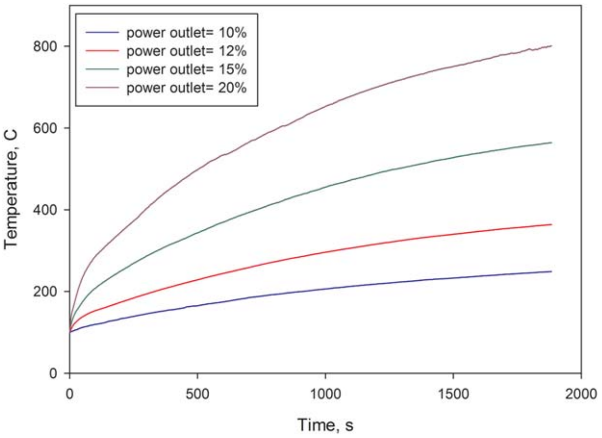

Figure 16. Effect of power outlet of the power supply on rate of heating of the sand particles; mass 10 g, size 149–212 μm, air pressure 207 kPa, and amplitude 6.4 cm.

[Color figure can be viewed in the online issue, which is available at wileyonlinelibrary.com.]

Fluidization Dynamics of Geldart's Group A and Group B Solid Particles. To compare fluidization dynamics of the Geldart's Group A and Group B particles, pellets of a porous commercial nickel-based steam reforming catalyst containing 63.7 wt % Al_2O_3, catalyst A, were crushed and sieved to prepare samples with particle sizes in the ranges 45–75 μm (representing Group A powders), 75–149 and 149–212 μm (representing Group B powders). Apparent and skeletal densities of the catalyst A were 1976 and 3305 kg/m^3, respectively.

An 8.5 g mass of catalyst A was agitated in the crucible at different actuator frequencies with 6.4 cm amplitude. Variations of $CV_{space,min}$ and power of dominant frequency with air pressure are illustrated in Figure 15. According to results displayed in Figure 15a, $CV_{space,min}$ for Group B particles stabilized with values below 0.15 at air pressures above 200 kPa, indicating catalyst particles were well distributed over the entire length of the crucible. However, with Group A particles, $CV_{space,min}$ was about 0.17 at the highest air pressure of 700 kPa: this indicated a distribution of the particles over the entire length of the crucible that was good but not as effective as with Group B particles; trends shown in Figure 15a suggest that an even distribution could have been achieved at higher air pressures.

Results of analysis of power of the dominant frequency shown in Figure 15b also prove poor mixing intensity for Group A catalyst particles in the crucible. Conversely, a trend similar to that for sand particles in Figure 14 was obtained for the two size distributions of Group B catalyst particles in Figure 15b: mixing intensity was maximized for

Table 2. Required Data for Heat Transfer Calculations

Sand Particles		$A_0\,(\mathrm{m}^2)=0.023$		$A_w\,(\mathrm{m}^2)=0.00614$	
$C_{\mathrm{p,s}}\left(\frac{\mathrm{J}}{\mathrm{kg.{}^{o}C}}\right)$	830	d_{o} (m)	0.0635	d_{w} (m)	0.0032
$\mathrm{m_s}$(kg)	0.01	l_{o} (m)	0.083	l_{w} (m)	0.0762

catalyst particles in the 149–212 μm range, at a lower actuator air pressure.

Attrition of Catalyst Particles. In regular fluidized beds, the gas distributor jets and the cyclones primarily cause attrition, with attrition caused by bubbles being much milder. Attrition is also expected in the jiggled bed reactor in particular due to shaking the reactor and collision between catalyst particles and between particles and reactor.

In fact, the jiggled bed reactor is a test reactor designed for screening and kinetic studies in batch-wise operation with very short reaction times rather than for continuous and long run operation tests; therefore, attrition should not be a serious issue with this reactor. Nonetheless, to investigate extension of particles attrition, pellets of the porous catalyst A were crushed and sieved to obtain size cuts with the Sauter-mean diameters of 742, 541, and 355 μm. Such quite coarse particles were prepared to better observe the attrition. A 8.5 g mass of these particles were agitated inside the crucible for 30 min with actuator air pressure of 345 kPa and amplitude of 6.4 cm; then the particle-size distribution was measured.

Size distribution of the three size cuts of the catalyst particles before agitation and after agitation is listed in Table 1 along with the Sauter-mean particle diameter. It must be pointed out that agitation tests were repeated for three times for each size cut and average data are reported here. It is obvious that the catalyst particles underwent attrition to some extent but the reduction in the Sauter-mean diameter of the catalyst particles was only between 8 and 28 μm for an agitation time of 30 min.

Optimization of Fluidization Dynamics—Heat Transfer Study

One of the main problems of the microreactors that are currently used to test catalysts is that, with endothermic reactions, poor heat transfer results in heat transfer surfaces that are at a much higher temperature than the catalyst bed, causing undesirable parasitic thermal cracking reactions. It is, therefore, important to check that in the JBR, the temperature difference between the heating surfaces and the catalyst bed is minimized without compromising the ability to transfer heat.

The ceramic crucible was loaded with 10 g of silica sand with a size distribution of 149–212 μm. The actuator was operated at air pressures of 138, 207, and 276 kPa and the reactor bed was heated up to 800°C by induction heating. The power supply was then switched off to let JBR cool down while the air cylinder was still vibrating.

Heat-transfer modeling

When the power supply is switched off, the temperature of the catalyst bed drops quickly due to heat loss from the reactor

$$m_{\mathrm{s}}C_{\mathrm{P,s}}\frac{dT_{\mathrm{s}}}{dt}=-h_{\mathrm{o}}A_{\mathrm{o}}(T_{\mathrm{s}}-T_{\infty}) \tag{4}$$

The heat losses can be characterized from h_0A_0. The temperature of the sand particles can be related to h_0A_0 by integrating Eq. 4. Setting a $=\frac{h_{\mathrm{o}}A_{\mathrm{o}}}{m_{\mathrm{s}}C_{\mathrm{P,s}}}$, Therefore,

$$\frac{T_{\mathrm{s}}-T_{\infty}}{T_{\mathrm{s},0}-T_{\infty}}=\exp\left(-a(t-t_0)\right) \tag{5}$$

During heating up of the catalyst bed in the JBR, the metal wires are heated by induction and heat is then transferred from the wires to the bed, where P is the power transferred to the bed. Heat is lost through the reactor wall, as during cooling

$$m_{\mathrm{s}}C_{\mathrm{P,s}}\frac{dT_{\mathrm{s}}}{dt}=P-h_{\mathrm{o}}A_{\mathrm{o}}(T_{\mathrm{s}}-T_{\infty}) \tag{6}$$

Estimation of T_{s} during the heating step can be achieved by integrating Eq. 6. Setting $b=\frac{P}{h_{\mathrm{o}}A_{\mathrm{o}}}$, Therefore,

$$T_{\mathrm{s}}=T_{\infty}+b+\left(T_{\mathrm{s},0}-T_{\infty}-b\right)\exp\left(-a(t-t_0)\right) \tag{7}$$

Parameters a and b can be estimated by regression of the temperature data during the cooling and heating steps. Parameters h_{o} and P can then be found from a and b. The heat-transfer coefficient, $\mathrm{h_w}$, from the heating wires to the bed can be estimated from the power transferred from the wires to the bed with Eq. 8

$$P=h_{\mathrm{w}}A_{\mathrm{w}}(T_{\mathrm{w}}-T_{\mathrm{s}}) \tag{8}$$

A_{o} and A_{w} are calculated with Eqs. 9 and 10

$$A_{\mathrm{o}}=2\times\pi\frac{d_{\mathrm{o}}^2}{4}+\pi d_{\mathrm{o}}l_{\mathrm{o}} \tag{9}$$

$$A_{\mathrm{w}}=8\times\left(\pi\frac{d_{\mathrm{w}}^2}{4}+\pi d_{\mathrm{w}}l_{\mathrm{w}}\right) \tag{10}$$

To calculate the heat-transfer coefficient h_{w}, however, the temperature difference between the wires and sand particles must be known. To do so, a label temperature indicator whose color turns into black color at a rated temperature was applied to one of the wires, and the reactor was heated up to temperatures below the rated temperature of the label, changing the reactor temperature in one degree Celsius intervals between successive experiments. Experiments were conducted until the label color turned black. The difference between the achieved reactor temperature and the rated temperature of the wire label was used in Eq. 8 to calculate the heat-transfer coefficient between the heating wires and the catalyst bed.

Results and discussion

Effect of the Delivered Power. Induction heating is a very fast heating method. However, if the power supply delivered its full power to the induction coil, the internal wires of the reactor could reach a very high temperature after a few seconds, resulting in a large temperature difference between the wires and the sand particles inside the reactor. To minimize the thermal stress on the reactor, and especially, on the ceramic crucible, reduced power should be delivered to heat up the reactor to reach the desired temperature.

Figure 16 shows how quickly the catalyst bed could be heated, starting from an initial temperature of 100°C. The

Table 3. Measured Temperatures on the Surface of Wires and Inside the Reactor

Power Level (%)	T_s (°C)	T_w (°C)	$(T_W - T_S)$ (°C)
10	198	204	6
12	205	210	5
15	246	249	3
20	247	249	2

controller was set in the open loop mode to see the effect of the power outlet of the power supply on heat transfer inside the ceramic crucible. The power level was varied between 10 and 20% of the maximum power. The reactor was vibrated at an actuator air pressure of 207 kPa with an amplitude of 6.4 cm. Figure 16 indicates that reaching a reactor temperature of 800°C requires a power of about 20% of maximum power.

Table 2 lists the heat capacity and mass of bed of sand particles as well as the dimensions of the heating surfaces. Regarding the eight wires inside the crucible, it can be concluded from the data in Table 2 that the total surface area of the wires is less than the external surface area of the crucible.

Table 3 shows the measured temperatures of the catalyst bed and of the surface of the heating wires for various power levels. The temperature difference between the wires and the bed was quite small, indicating that heat transfer was very effective. Surprisingly, the temperature difference between the wires and the bed decreased as the power level was increased. This may be caused by the controller scheme. When the power level is 10%, the induction system does not deliver a constant power of 10% of its maximum power; instead, it delivers full power for 10% of the time. The intermittent nature of the power delivery is, therefore, exacerbated when the nominal power level is low. Since the method used in this study measured the maximum temperature reached by the wires over a whole run, the wire temperature will be overestimated by a larger margin as heating becomes more intermittent.

Figure 17 shows that there is a linear relationship ($R^2=0.9962$) between the power level, that is, the power supplied to the induction coil, and the power actually transferred from the heating wires to the catalyst bed. This confirms that the model and calculation procedure used to estimate the power transferred from the wires to the bed gave consistent results.

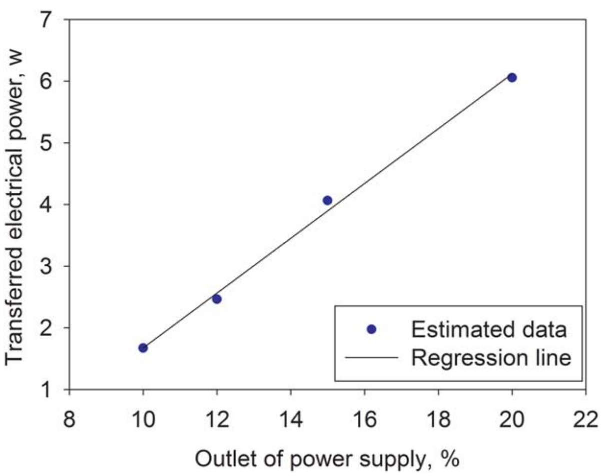

Figure 17. Consumed power inside the reactor vs. partial power outlet of the power supply.

[Color figure can be viewed in the online issue, which is available at wileyonlinelibrary.com.]

Table 4. Consumed Power, Heat Loss Heat-Transfer Coefficient, and Heat-Transfer Coefficient Between Wires and Bed; Air Pressure 207 kPa, Sand Particles 10 g

Power Level (%)	$h_0\ \left(\frac{\text{w}}{\text{m}^2\cdot{}^\circ\text{C}}\right)$	P (w)	$h_w\ \left(\frac{\text{w}}{\text{m}^2\cdot{}^\circ\text{C}}\right)$
10	0.265	1.671	45
12	0.257	2.462	80
15	0.270	4.063	220
20	0.269	6.058	493

The heat-transfer coefficients for the heat losses and between the heating wires and the bed were calculated from the experimental data for various power levels, using the method described earlier (Table 4). As expected, the heat-transfer coefficient for the heat losses is independent of the power level.

The heat-transfer coefficient between the heating wires and the bed increased dramatically with the power level (Table 4). As discussed earlier, the wire temperature would be overestimated by a larger margin at lower power levels, which would then result in an erroneous heat-transfer coefficient. The heat-transfer coefficient obtained at the higher power level of 20% is more realistic and is more relevant to this study, since it provided a steady-state temperature of around 800°C, a typical temperature for gasification reactions. According to the correlation from Molerus et al.[21] for heat transfer between a tube and a fluidized bed, the heat-transfer coefficient obtained at a power level of 20% would correspond to a ratio of fluidization velocity to minimum fluidization velocity of about 30, which is typical of a well-bubbling fluidized bed. This confirms the excellent quality of the fluidization achieved with the JBR.

Effect of Frequency of the Pneumatic Actuator. Effect of the actuator air pressure on heat transfer was investigated at power outlet of 20%. Figure 18 shows how quickly the bed temperature increased for different air pressures applied to the actuator piston. The temperature rose more slowly at higher air pressures. Since, as shown in Figure 9, the

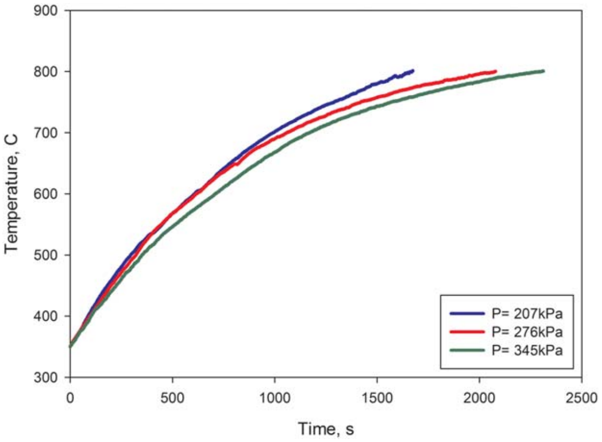

Figure 18. Effect of the actuator air pressure on the rate of temperature rise inside the reactor during the heating step; power outlet 20%, mass of sand particles 10 g, and amplitude 6.4 cm.

[Color figure can be viewed in the online issue, which is available at wileyonlinelibrary.com.]

Table 5. Consumed Power, Heat Loss Heat-Transfer Coefficient, and Heat-Transfer Coefficient Between Wires and Sand Particles; Power Outlet 20%, Sand Particles 10 g, and Amplitude 6.4 cm

Air pressure (kPa)	$h_0\left(\frac{\mathrm{w}}{\mathrm{m}^2.^{\circ}\mathrm{C}}\right)$	P (w)	$h_\mathrm{w}\left(\frac{\mathrm{w}}{\mathrm{m}^2.^{\circ}\mathrm{C}}\right)$
207	0.269	6.058	493.27
276	0.290	6.054	492.91
345	0.299	5.969	486.06

frequency at which the bed level fluctuated increased with the air pressure, this suggests that operating with a lower frequency of bed pulsations would maximize heat transfer between heating wires and bed.

The results shown in Figure 18 are confirmed in Table 5, which shows that the heat-transfer coefficient between the wires and the bed decreased slightly as the air pressure and, hence, the bed frequency increased. Interestingly, this means that the heat-transfer coefficient between the wires and the bed is at its maximum when the bed agitation is maximized: Figure 13b shows that for the bed mass and particle-size distribution used in the heat transfer experiments, the most intense bed agitation was obtained at an air pressure of just above 200 kPa.

Conversely, Figure 19 shows that the air pressure had little effect on the rate at which the bed temperature dropped once heating had been switched off. This indicates that, as expected, the heat losses are controlled by the external heat transfer between the outer crucible wall and the ambient air, and are practically independent of the heat-transfer coefficient between the bed and the inner crucible wall.

To investigate whether the induction heating system implemented with the JBR is effective and rapid enough to compensate the heat consumed by the endothermic reactions, water injection was used for testing, since its vaporization is endothermic; 4 mg droplets of water were injected into the reactor to simulate heat consumption by endothermic reactions. As shown in Figure 20, the bed temperature dropped by less than 2°C for each droplet and then it took less than 5 s for the bed to recover its initial temperature. The negligible temperature drop and the fast recovery observed prove that the developed induction heating technique is very effective for the study of gasification reactions.

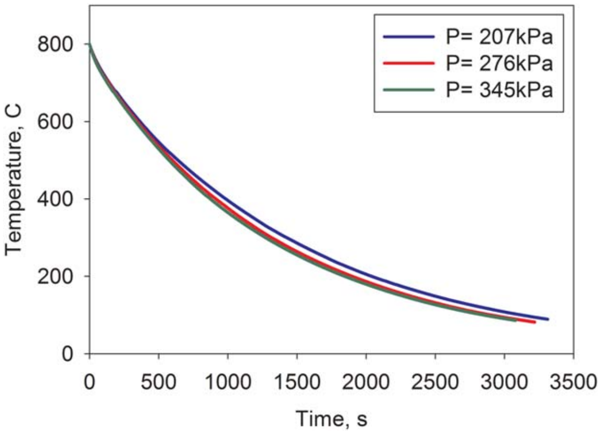

Figure 19. Effect of air pressure of the actuator on rate of temperature drop inside the reactor during the cooling step; power outlet 20%, mass of sand particles 10 g, and amplitude 6.4 cm.

[Color figure can be viewed in the online issue, which is available at wileyonlinelibrary.com.]

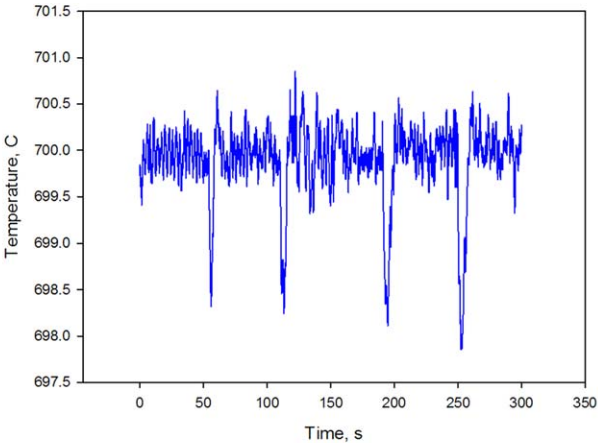

Figure 20. Temperature recovery for endothermic reactions taking place in the JBR.

[Color figure can be viewed in the online issue, which is available at wileyonlinelibrary.com.]

Conclusions

The JBR is a batch microreactor with performance characteristics that make it suitable to test gasification catalysts. A linear pneumatic actuator was successfully designed to achieve fluidization conditions in the reaction zone of the JBR, without using any fluidization gas. A new induction heating system was designed and implemented to provide a uniform distribution of heat to the bed with a very small temperature difference between the heating surface and the bed. Fluidization and heating of the catalyst bed can, thus, be achieved in a completely noninvasive manner.

A new image processing technique was developed to monitor the fluidization dynamics of the catalyst bed. A signal processing technique was used to optimize amplitude and frequency of the pneumatic actuator to achieve the best fluidization conditions. The size distribution and mass of the catalyst particles were also optimized to enhance fluidization.

Heat transfer studies showed that induction heating provides a minimum temperature difference between the heating wires and the catalyst bed. The maximum fluidization intensity of the bed corresponds to the highest heat-transfer coefficient between the heating wires and the catalyst bed.

Acknowledgments

The authors gratefully acknowledge the financial support of the Natural Sciences and Engineering Research Council of Canada (NSERC), of the Minister of Research and Innovation of Ontario and Agriculture and AgriFood Canada. The authors would also like to thank Dr. Marcel Schlaf of the University of Guelph for suggesting that JBR could also stand for "James Bond Reactor", since the reactor is "shaken, not stirred".

Notation

A = Amplitude, cm
A_o = External surface area of the ceramic crucible, m^2
A_P = Cross section area of the piston, m^2
A_{rod} = Cross section area of one rod, m^2
A_w = Surface area of all internal inconel wires, m
$a_{P,ext}$ = Acceleration of the piston during extension mode, $\frac{m}{s^2}$
$a_{P,ret}$ = Acceleration of the piston during retraction mode, $\frac{m}{s^2}$
$C_{P,s}$ = Specific heat of the sand particles, $\frac{J}{kg.°C}$
CV_{space} = Coefficient of variation of colour change of pixels on picture i at time j
CV_{time} = Coefficient of variation of colour change of pixel i on all pictures during the time period of j
$CV_{space,\ min}$ = Maximum uniform distribution of the particles in the entire length of the reactor
d_o = O.D. of the ceramic crucible, m
$d_{p,AAG}$ = Sauter-mean diameter of catalyst particle after agitation, μm
$d_{p,BAG}$ = Sauter-mean diameter of catalyst particle before agitation, μm
d_w = Diameter of an internal inconel wire, m
F = Force, N
$f_{actuator}$ = Frequency of the actuator, Hz
f_{bed} = Frequency of the bed, Hz
$f_{bed,d}$ = Dominate frequency of the bed, Hz
g = 9.806 acceleration constant of the ground, $\frac{m}{s^2}$
h_o = Heat-transfer coefficient of heat loss through wall of the ceramic crucible, $\frac{w}{m^2.°C}$
h_w = Heat-transfer coefficient between internal inconel wires and bed of the sand particles, $\frac{w}{m^2.°C}$
Δh = Distance between the reed switches
l_o = External length of the ceramic crucible, m
l_w = Length of an internal inconel diameter, m
m = Mass of sand particles, g
m_R = Mass of the reaction zone, kg
m_s = Mass of bed of the sand particles, kg
N_i = Number of pixels in picture i
N_j = Number of pictures in time period j
P = Power consumed to heat up internal inconel wires
P_{air} = Pressure of compressed air, Pa
$\overline{P}_{air}$ = Average pressure of the compressed air during the piston brake, Pa
T_s = Temperature of bed of the sand particles, °C
T_w = Temperature of surface of the internal inconel wires, °C
T_∞ = Room temperature, °C
$v_{P,ext}$ = Velocity of the piston during extension mode, $\frac{m}{s}$
$v_{P,ret}$ = Velocity of the piston during retraction mode, $\frac{m}{s}$
Δx_{ext} = Brake length at the end of extension mode, m
Δx_{ret} = Brake length at the end of retraction mode, m
$y_{i,j}$ = Color value of a pixel in picture i at time j

Greek letters

σ = Standard deviation of color value
μ = Average of color value

Literature Cited

1. Latifi M. *Gasification of Bio-Oils to Syngas in Fluidized Bed Reactors*, Ph.D. Thesis, London, Ontario: Chemical and Biochemical Engineering, Western University, 2012.
2. Latifi M, Ferrante L, Briens C, Berruti F. Effect of temperature and residence time on the thermal cracking of bio-oil for syngas production. In: ECI Conference, Bioenergy II, Rio de Janeiro, Brazil,March 2009.
3. Imhof P, Baas M, Gonzalez JA. Fluid catalytic cracking catalyst evaluation: the short contact time resid test. *Catal Rev—Sci Eng.* 2004;46(2):151–161.
4. Berty JM. Testing commercial catalysts in recycle reactors. *Catal Rev—Sci Eng.* 1979;20(1):75–96.
5. Kraemer DW, de Lasa HI. Catalytic cracking of hydrocarbons in a riser simulator. *Ind Eng Chem Res.* 1988;27(11):2002–2008.
6. Ozturk Z, Merklin JF. Fast pyrolysis of cellulose with reactive methane gas in a single-pulse shock tube. *J Appl Polym Sci.* 1994;52(6): 747–753.
7. Boutin O, Ferrer M, Lede J. Radiant flash pyrolysis of cellulose—evidence for the formation of short life time intermediate liquid species. *J Anal Appl Pyrolysis.* 1998;47(1):13–31.
8. Drummond A-RF, Drummond IW. Pyrolysis of sugar cane bagasse in a wire-mesh reactor. *Ind Eng Chem Res.* 1996;35(4):1263–1268.
9. Rudnev V, Loveless D, Cook RL, Black M. *Handbook of Induction Heating*, New York, NY: Marcel Dekker, Inc., 2002.
10. Davies J. *Conduction and Induction Heating*. London, UK: Peter Peregrinus Ltd., 1990.
11. Li Z, Xu S, Zhang J, Chang Y, Ni J, Zhou X, Hao Y. Finite element analysis of the temperature field in a vertical MOCVD reactor by induction heating. *J Semicond.* 2009;30(11):113004-1–113004-5.
12. Rastogi A, Svrcek WY, Behie LA. Novel microreactor with quench system for kinetic study of propane pyrolysis. *AIChE J.* 1988;34(9): 1417–1422.
13. Tsai WT, Lee MK, Chang YM. Fast pyrolysis of rice straw, sugarcane bagasse and coconut shell in an induction-heating reactor. *J Anal Appl Pyrolysis.* 2006;76(1–2):230–237.
14. Rohani S, Latifi M, Ferrante L, Briens C, Berruti F. A novel induction heating microreactor for gasification catalyst-testing. In: 2nd GPE-EPIC conference. Venice, Italy, June 14–17, 2009.
15. Kastens ML, Hirst LL, Dressier RG. An american fischer-tropsch plant. *Ind Eng Chem.* 1952;44(3):450–466.
16. Vorontsov AV, Kozlov DV, Smirniotis PG, Parmon VN. TiO_2 photocatalytic oxidation: III. Gas-phase reactors. *Kinet Catal.* 2005; 46(3):437–444.
17. Klusacek K, Schneider P. Stationary catalytic kinetics via surface concentrations from transient data. *Chem Eng Sci.* 1982;37(10): 1523–1528.
18. Richter M, Mrkwitschka G, Ohlmann G. An all-glass vibration mixed reactor for gas/solid catalyzed reactions. *React Kinet Catal Lett.* 1987;34(1):21–27.
19. Squires AM. Chemical process opportunities for vibrated powders 1. In the laboratory. *Powder Technol.* 2004;147(1–3):1–9.
20. Nelson RJ, Flakker CL, Muggli DS. Photocatalytic oxidation of methanol using titania-based fluidized beds. *Appl Catal B.* 2007; 69(3–4):189–195.
21. Molerus O, Burschka A, Dietz S. Particle migration at solid surfaces and heat transfer in bubbling fluidized beds-II. Prediction of heat transfer in bubbling fluidized beds. *Chem Eng Sci.* 1995;50(5):879–885.

Appendix: Sizing the Air Cylinder

The frequency of the pneumatic actuator is a function of internal volume of the air cylinder, flow rate of the air, alternation timing of the solenoid valve, and weight of the reaction zone at given amplitude. In addition, amplitude of the pneumatic actuator must be long enough for the solid particles to be fluidized in the entire length of the ceramic crucible. Maximum achievable amplitude is, however, limited by two ends of the air cylinder which is determined by the maximum possible distance between the RS. It has been seen in practice that, in contrary to general expectation, distance between the RS must be way less than the desired length of the amplitude so that the piston does not hit the air cylinder. In other words, although the piston is supposed to be stopped where a reed switch senses the magnet on the piston, due to fast speed of the piston and delay time of the alternation action by the solenoid valve, the piston tends to keep moving past the reed switch until it either faces the opposite entering compressed air or hits the cylinder. We call this action "the piston brake" and the extra distance travelled beyond the reed switch is called "the brake length" (Figure A1) which is an important design parameter to size the air cylinder. Therefore, it is crucial to know the distance between the RS on the external surface of the air cylinder to control the amplitude of vibration.

The brake length at the end of extension mode and retraction mode can be estimated from the equations A1 and A2

$$\Delta x_{ext} = -\frac{v_{P,ext}^2}{2a_{P,ext}} \tag{A1}$$

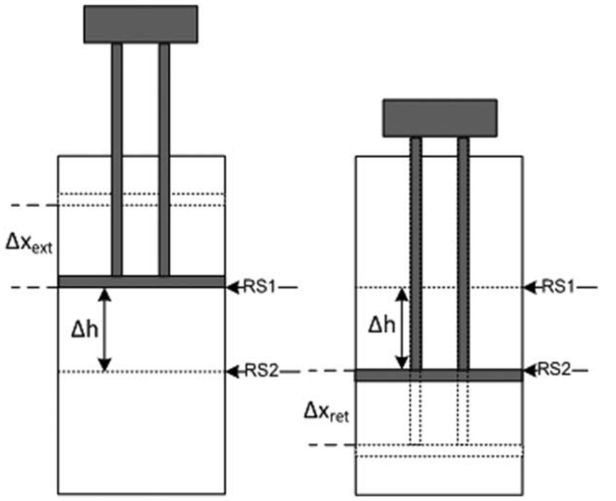

Figure A1. Schematic of the flat air cylinder with the dual rods presenting position of the RS and the brake length (Δ*x*) at the end of extension (left) and retraction (right) modes.

$$\Delta x_{\text{ret}} = \frac{v_{\text{P,ret}}^2}{2a_{\text{P,ret}}} \tag{A2}$$

v_{P} is estimated from the thermodynamics' first law (assuming weight of the piston is negligible) when the stagnant piston in front of a reed switch is pushed or pulled and then travels the length between the RS (Δh):

$$m_{\text{R}} g \Delta h + \frac{1}{2} m_{\text{R}} v_{\text{P}}^2 = F \Delta h \tag{A3}$$

Where at extension mode

$$F = P_{\text{air}} A_{\text{P}} - m_{\text{R}} g \tag{A4}$$

While at retraction mode

$$F = P_{\text{air}} \left(A_{\text{p}} - 2A_{\text{rod}}\right) + m_{\text{R}} g \tag{A5}$$

During the piston brake, pressure of air reduces dramatically until it becomes zero because its flow is stopped. Applying the Newton's second law for the brake length, a_{P} can be estimated as below:

At extension mode

$$(P_{\text{air}} A_{\text{P}} - m_{\text{R}} g) dt = m_{\text{R}} dv_{\text{p,ext}} \tag{A6}$$

Assuming $\bar{P}_{\text{air}}$ as the average value of the reducing pressure of compressed air,

$$a_{\text{P,ext}} = \frac{\bar{P}_{\text{air}} A_{\text{P}} - m_{\text{R}} g}{m_{\text{R}}} \tag{A7}$$

Similarly, at retraction mode

$$(P_{\text{air}} (A_{\text{P}} - 2A_{\text{rod}}) + m_{\text{R}} g) dt = m_{\text{R}} dv_{\text{p,ret}} \tag{A8}$$

$$a_{\text{P,ret}} = \frac{\bar{P}_{\text{air}} (A_{\text{P}} - 2A_{\text{rod}}) + m_{\text{R}} g}{m_{\text{R}}} \tag{A9}$$

Finally, if we assume that $\bar{P}_{\text{air}}$ is almost zero in Eqs. A7 and A9 which is a true assumption, the brake lengths will be calculated from the equations below

$$\Delta x_{\text{ext}} = -\frac{(P_{\text{air}} A - m_{\text{R}} g) \Delta h - m_{\text{R}} g \Delta h}{m_{\text{R}} g} \tag{A10}$$

$$\Delta x_{\text{ret}} = \frac{(P_{\text{air}} (A - 2A_{\text{rod}}) - m_{\text{R}} g) \Delta h - m_{\text{R}} g \Delta h}{m_{\text{R}} g} \tag{A11}$$

Equations A10 and A11 illustrate that the brake lengths are dependent on mass of the reaction zone, distance between the RS and bore size of the air cylinder at a given pressure of the compressed air. Effect of these parameters on the brake lengths were investigated to find the optimum size of the air cylinder.

Manuscript received Dec. 23, 2013, and revision received Mar. 31, 2014.